# Journal of Physics: Photonics



#### **OPEN ACCESS**

#### RECEIVED

24 May 2025

#### REVISED

9 June 2025

# ACCEPTED FOR PUBLICATION

6 August 2025

#### PUBLISHED

14 August 2025

Original Content from this work may be used under the terms of the Creative Commons Attribution 4.0 licence.

Any further distribution of this work must maintain attribution to the author(s) and the title of the work, journal citation and DOI.



#### **PAPER**

# Model of *in-situ* focusing of extreme ultraviolet high-order harmonics from a nanostructured MgO surface

Parnia Bastani<sup>1,5</sup>, Aleksey Korobenko<sup>1</sup>, Vedran Jelic<sup>1,5</sup>, Jesse Thompson<sup>2,3</sup>, Anton Rudenko<sup>2,3</sup>, Francois Légaré<sup>5</sup>, Lora Ramunno<sup>2,3,4</sup> and Giulio Vampa<sup>1,2,3,4,\*</sup>

- <sup>1</sup> Joint Attosecond Science Laboratory, National Research Council of Canada & University of Ottawa, Ottawa K1N 5A2, Canada
- <sup>2</sup> Joint Center for Extreme Photonics, National Research Council of Canada & University of Ottawa, Ottawa, Canada
- <sup>3</sup> NEXQT Institute, University of Ottawa, 25 Templeton Street, Ottawa, Ontario K1N 6N5, Canada
- Department of Physics, University of Ottawa, Ottawa, ON K1N 6N5, Canada
- Advanced Laser Light Source (ALLS), Institut National de la Recherche Scientifique (INRS-EMT), 1650 Boulevard Lionel-Boulet, Varennes, Québec J3X 1P7, Canada
- \* Author to whom any correspondence should be addressed.

E-mail: Giulio.Vampa@uottawa.ca

Keywords: high harmonic generation, extreme ultraviolet radiation, Fresnel zone plate, metasurface

### **Abstract**

We present a numerical model for the *in-situ* generation and focusing of extreme-ultraviolet (XUV) high harmonics via a Fresnel zone plate etched into a dielectric (MgO) surface. Our simulations show that propagation of the intense infrared field driving high-harmonic emission through the etched surface rings introduces well-controlled amplitude and phase modulations of the XUV field emitted from the surface itself that enhance the focusing efficiency up to 25%, beyond that of both conventional amplitude-modulated transmission XUV zone plates as well as ideal phase-only zone plates. Rings with a width comparable to the wavelength of the infrared driver exhibit strongest XUV emission with a larger phase modulation due to enhancement of the infrared field. On the contrary, a smooth phase modulation is achieved in the outskirts of the zone plates, where the width of the rings is much smaller than the infrared driving wavelength. These findings highlight the potential of sub-wavelength metasurface design in optimizing nanostructured optical elements for XUV nano-spectroscopy and on-chip XUV beam shaping.

# 1. Introduction

Vacuum and extreme ultraviolet (XUV) light is radiation with photon energy higher than  $\sim 10 \, \text{eV}$ , corresponding to a wavelength shorter than  $\sim 120 \, \text{nm}$ . It is finding numerous applications for spectroscopy with chemical and elemental specificity [1], nanoscale imaging [2–4] and photolithography [5]. Yet, significant difficulties exist in manipulating XUV light because nearly every material is opaque to it, which excludes the use of bulk transmission optics such as lenses which are commonly used in the visible spectral region. Alternatives exist that rely on suitable thin-film materials for multilayer Bragg mirrors [5] and membrane waveplates [6], as well as conventional diffractive optical elements such as gratings and Fresnel zone plates [7]. A recent innovative approach utilizes waveguiding in nanoholes [8], an approach similar to that utilized to boost ultraviolet high harmonics from a thin grating structure [9].

The generation of XUV light is also rather challenging, especially when temporal and/or spatial coherence is desired. In the realm of coherent XUV sources, the front-runner method is high-order harmonic generation, an extremely non-linear process that occurs in gases [10, 11], liquids [12] and solids [13, 14] when subjected to intense femtosecond infrared laser fields. The outcome of the interaction is a comb of harmonics of the infrared driver's frequency that can extend to very high orders, generating photons with energies upwards of hundreds of eVs in gases [15–18], and up to  $\sim$  30 eV in solids [19].

The discovery of solid-state high-harmonic emission in 2011 [13] opened unprecedented opportunities to control high-harmonic emission with nanostructured surfaces. Early demonstrations utilized three-dimensional semiconducting [20] and dielectric cones [21], as well as metallic plasmonic

nanoantennas [22] to enhance the infrared field either by adiabatic focusing or by resonant enhancement. Shaping the infrared field to control the non-linear high-harmonic emission was later extended to more sophisticated metasurfaces that utilized Fano-type resonances [23], bound states in the continuum [24] and dielectric resonant antennas [25]. The nanostructures emitted high harmonics more efficiently than the unpatterned surface due to the field enhancement, and with shaped far-field profiles due to the periodic arrangement. A suitable arrangement of perpendicularly-oriented nanoantennas also results in the emission of circularly polarized high harmonics, whereas bulk could only emit linearly polarized ones [26]. Another approach for increasing the high-harmonic efficiency pioneered the use of vacuum channels between sub-infrared-wavelength ridge waveguides to boost the emitted high-harmonic flux without shaping the infrared field [9]. Propagation of the harmonics in the channel allowed buildup over hundreds of nanometres rather than the  $\sim$  5 nm extraction depth of the unpatterned surface. All these examples highlight the potential in utilizing nanostructured surfaces to simultaneously emit and control high-harmonic emission. This *in-situ* approach has the advantage that additional functionalities, such as structured illumination of both spatial and polarization degrees of freedom, can be integrated in one optical element, without the need of external (potentially lossy) optics.

All previous examples, except one [21], utilized metallic and semiconducting materials that are amenable to nanofabrication. In these materials, harmonic emission is limited to the visible and deep-ultraviolet spectral regions. Recently, we demonstrated the ability to pattern the surface of a dielectric crystal, MgO, that is an efficient emitter of high harmonics in the XUV spectral region [27], up to  $\sim$  25 eV [28]. Patterning one-and two-dimensional gratings resulted in efficient diffraction of the 7th harmonic of a Ti:Sapphire laser (114 nm wavelength), demonstrating spatially-structured XUV emission from solids for the first time [29]. By etching a Fresnel zone plate on the surface of MgO, we demonstrated simultaneous generation and focusing of the same harmonic with high numerical apertures (NA) of 0.18 and 0.35, down to a focus size of 150 nm with up to  $\sim$  20% efficiency [30].

In this work we present a theoretical model that underpins those results. Our model is based on separating the infrared propagation through the nanostructured surface from the high-harmonic emission and its subsequent propagation to the focal plane. The model confirms, somewhat surprisingly, that zone plate patterns—which are designed to satisfy linear-optical requirements—can be made even more effective at producing nanoscale foci when operating in the non-linear regime of high-harmonic emission. Our results will guide the design of improved XUV non-linear metasurfaces with better focusing qualities and added functionalities.

The manuscript is organized as follows. In section 2 we explain the working principle of the non-linear zone plate metasurface; in section 3 we detail the results of each step of the modeling for a zone plate with NA = 0.35; in section 4 we analyze the dependence of the performance on the etch depth; in section 5 we dissect the results to understand the relative roles of XUV amplitude and phase modulations across the plate; in section 6 we demonstrate that the quality of the focus is maintained, if not improved, at an even higher NA = 0.5; and in section 7 we draw the conclusions.

# 2. Description of the model

The working principle is based on reshaping the phase of the intense infrared field that drives the high-harmonic generation process as it propagates through the nanoscale features of the surface. It is depicted in figure 1. An intense infrared driver (red lines), at a wavelength of 800 nm, propagates within the MgO substrate through the nanostructured surface and exits on the vacuum side. High-harmonic radiation (purple vertical lines) is generated throughout the material, but owing to the short absorption length of above-bandgap radiation (MgO bandgap is 7.8 eV), only light generated within  $\sim$  5 nm from the exit surface can escape the material and contribute to the detected signal, and is therefore considered in the model. Crucially, XUV light emitted at the bottom of the trenches ( $E_{\rm XUV}^{\rm trench}(z=-h)$ ) is generated with a different phase than that emitted at the top of the ridges ( $E_{\rm XUV}^{\rm ridge}(z=0)$ ) because the infrared driver accumulates a propagation phase going through the ridge that, for a bulk material, is  $\Delta\phi_{\rm IR}^{\rm ridge}=\phi_{\rm IR}^{\rm ridge}(z=0)-\phi_{\rm IR}^{\rm ridge}(z=-h)=2\pi\,nh/\lambda_0$ , where h is the etch depth,  $\lambda_0=800$  nm is the driver's wavelength and n=1.728 is the refractive index of MgO at the driver's wavelength. Hereafter we call the z=-h and z=0 planes the 'bottom plane' and 'top plane', respectively. High-harmonic radiation generated at either plane inherits the driver's phase, multiplied by the harmonic order m. In addition, XUV radiation generated in the trench accumulates a phase delay as it propagates to the top plane in the vacuum channel that is

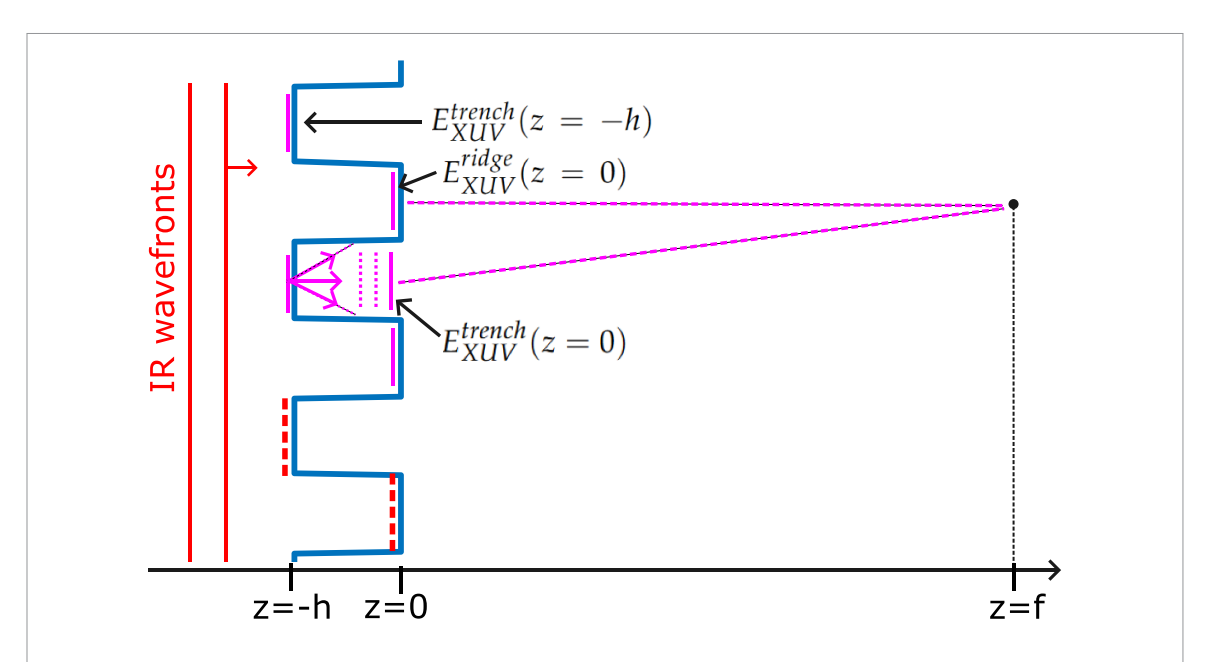


**Figure 1.** Schematics of the concept and geometry. Step 1: the IR wavefront (red lines) irradiates the etched MgO(100) surface (blue line, etch depth h) propagating from inside the MgO substrate. Step 2: XUV radiation (purple vertical lines) is generated just below the bottom of the trenches ( $E_{\text{XUV}}^{\text{trench}}(z=-h)$ ) and the top of the ridges ( $E_{\text{XUV}}^{\text{ridge}}(z=0)$ ). Radiation in the trenches propagates towards the top (z=0) in the vacuum channel between adjacent ridges ( $E_{\text{XUV}}^{\text{trench}}(z=0)$ ). Radiation that propagates at large angles and encounters the channel sidewall is considered absorbed by MgO. Step 3: the combined XUV field at z=0 is propagated to the focus, at z=f. The IR field in figure 2 is shown by merging the fields at the bottom of the trenches with those at the top of the ridges (red-dotted lines).

 $\Delta\phi_{
m XUV}^{
m trench}=\phi_{
m XUV}^{
m trench}(z=0)-\phi_{
m XUV}^{
m trench}(z=-h)=2\pi\,mh/\lambda_0$ . We call this field  $E_{
m XUV}^{
m trench}(z=0)$ . Thus, due to the patterning, the high-harmonic emission at a plane just beyond the top plane exhibits a phase modulation of:

$$\Delta \phi = m \Delta \phi_{\rm IR}^{\rm ridge} - \Delta \phi_{\rm XUV}^{\rm trench} = 2\pi \, m \, (n-1) \, h / \lambda_0 \tag{1}$$

If the phase modulation is structured at the top plane like that of a Fresnel zone plate [7], the emitted XUV will focus according to the zone plate design, with a diffraction efficiency that depends on the phase modulation  $\Delta\phi$ . Importantly, the phase modulation of the XUV field is non-zero even if the infrared is not modulated at all (e.g. if the infrared phase at the bottom and top planes is equal), which would result in the XUV radiation emitted with the same phase at the bottom and top planes, because  $\Delta\phi_{\rm XUV}^{\rm trench}\neq 0$  as long as  $h\neq 0$ —it represents propagation of the XUV in the vacuum channel. This is particularly important when the features (the zone plate rings) become smaller than the driver's wavelength in the material, as will be shown in this work.

Our modeling is composed of three separate steps that are based on this working principle:

- (i) Propagation of the infrared field through the structure is simulated with the finite-difference time-domain method using a commercial software (Lumerical). The electric field at the bottom and top planes are extracted from the simulation.
- (ii) The high-harmonic polarization at each plane is calculated with an empirical model from the complex electric field obtained at step 1. High-harmonic radiation at the bottom plane is propagated a distance *h* to the top plane, and merged with the radiation generated at the top plane. This yields the phase and amplitude modulated XUV at the MgO exit plane.
- (iii) The merged XUV field is propagated to the focus.

In the next section we present the results for a zone plate with NA of 0.35.

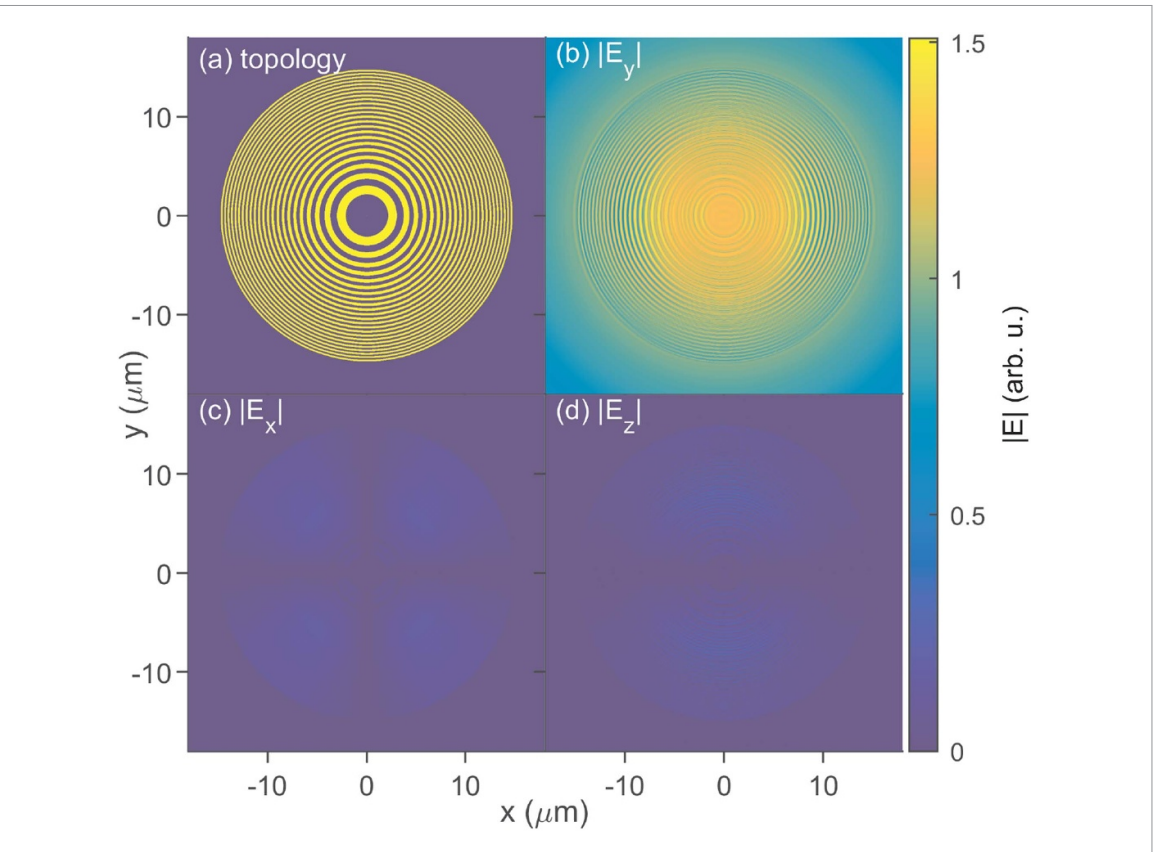


**Figure 2.** (a) View of the simulated topology in the (x, y) plane at z = 0 (just inside MgO). Yellow areas correspond to MgO, blue areas to vacuum. (b)–(d) Cartesian components of the absolute value of the infrared field inside MgO, along the corrugated profile shown as red-dotted line in figure 1, normalized to the input electric field. The source is polarized along  $\hat{y}$ , and  $E_y$  remains the dominant component.

# 3. Modeling of NA = 0.35 zone plate

The zone plate presented in this section has diameter of 30  $\mu$ m, focal length of 40  $\mu$ m, and etch depth h = 60 nm.

# 3.1. Step 1: infrared propagation

The geometry of the simulation is shown in figure 2(a). It consists of a semi-infinite MgO substrate where concentric rings are etched into the top (exit) surface to a constant depth h. The radii of the rings are chosen according to the usual zone plate equation [7]:

$$r_l = \sqrt{l\lambda_m f + (l\lambda_m/2)^2} \tag{2}$$

where  $\lambda_m = \lambda_0/m$  is the harmonic wavelength and  $l = \{0, 1, \dots N\}$  is an integer up to the highest zone. A Gaussian source with an intensity profile with  $1/e^2$  waist radius  $w_0 = 30 \,\mu\text{m}$ , pulse duration of 50 fs, linearly polarized along the  $\hat{y}$  direction, is launched from 1.6  $\mu$ m below the etched surface, inside MgO, towards positive  $\hat{z}$ . The electric field at the top and bottom planes is monitored at the 800 nm wavelength. Figures 2(b)–(d) show the amplitude of the y, x and z components of the electric field along the corrugated MgO surface (red-dashed line in figure 1), obtained by merging the fields at the bottom and top planes, 1 nm inside MgO (considered to be nominally z = 0). The input polarization ( $E_y$ ) remains dominant across the structure, with minor contributions from the longitudinal component  $E_z$  and the second transverse component  $E_x$ . The latter arises when the trenches are skewed relative to the input polarization. The former is present only when the trenches align perpendicular to the input polarization, which is expected since this geometry corresponds to TM excitation of waveguides, where longitudinal fields develop inside [31]. Because these components are small, in the following only the  $E_y$  component is utilized for modeling harmonic emission.

Both amplitude and phase of the infrared field show significant variations across the plate. The phase at z = 0 is shown in figure 3(a), with horizontal and vertical lineouts across the center shown in panel (b) with

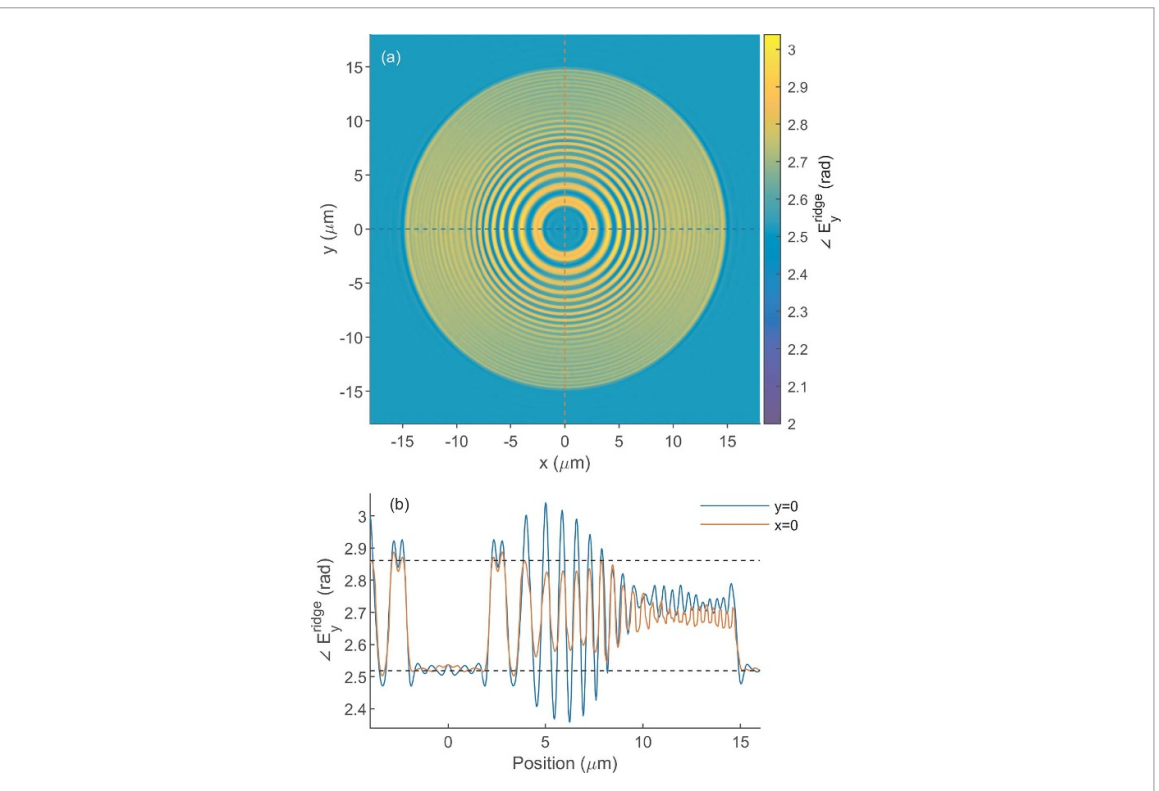


**Figure 3.** (a) Infrared phase of  $E_y(z=0)$ . (b) Lineouts across the origin. Amplitude enhancement in the waveguiding region corresponds to a phase modulation larger than that expected from bulk. The phase modulation and enhancement are larger for polarization parallel to the trenches (y=0), then for perpendicular (x=0).

blue and red lines, respectively. Three different regions can be identified, depending on the ratio of the laser wavelength in the material ( $\lambda_0/n=463$  nm) and the width of the rings ( $\Delta r=r_l-r_{l-1}$ ):

- (i)  $\Delta r > \lambda_0/n$ , occurring from the center of the plate to the first ring  $(l=3, \Delta r=620 \, \mathrm{nm})$ . Here, the field amplitude is similar to that of the input field and rather homogeneous. The phase modulation between adjacent ridges and trenches well matches that expected from equation (1), which assumes propagation through 'bulk' features and is indicated by the black dashed lines in figure 3(b). Thus, in this region the material behaves like bulk.
- (ii)  $\Delta r \sim \lambda_0/n$ , occurring approximately between the second and seventh rings ( $l \simeq 4$  to 14,  $\Delta r = 556$  to 328 nm). The amplitude is considerably enhanced inside the ridges, more so along the  $\hat{x}$  direction. We posit that waveguiding or scattering effects lead to this enhancement. Specifically, the reduction in the number of supported modes as the ring width shrinks can lead to better confinement and field enhancement. The asymmetry along  $\hat{x}$  and  $\hat{y}$  points to a polarization-dependent coupling for alignment of the trenches either parallel or perpendicular to the input polarization, which corresponds to either TE or TM excitation for the trenches along the two axes. The two coupling geometries are known to support modes at different waveguide widths, which explains the  $\hat{x} \hat{y}$  asymmetry. The large field enhancement along  $\hat{x}$  coincides with a larger phase modulation than in the bulk region, as shown by the blue line in figure 3(b).
- (iii)  $\Delta r < \lambda_0/n$ , occurring beyond the seventh ring (l > 15,  $\Delta r = 262$  to 164 nm). Here, the amplitude of  $E_y$  (figure 2(b)) becomes more uniform and the phase step reduces, and both remain largely independent of the position across the rest of the plate (i.e. on the width of the rings). In this region the infrared field couples to sub-wavelength structures. This is the regime where metasurfaces operate [32, 33]. In metaoptics, the infrared field amplitude and phase can be controlled with the geometry of individual sub-wavelength meta-atoms, a strategy that has proven very successful in metasurface design and has resulted in outstanding technological advances, such as for the development of metalenses with properties superior to those of standard bulk lenses [34, 35]. Designing a nonlinear XUV metasurface will be the scope of future work.

As we have shown here, the XUV zone plate encompasses optics at all scales, from bulk optics  $(\Delta r > \lambda_0/n)$  towards the center of the plate, to waveguide/scattering optics  $(\Delta r \sim \lambda_0/n)$  half-way through

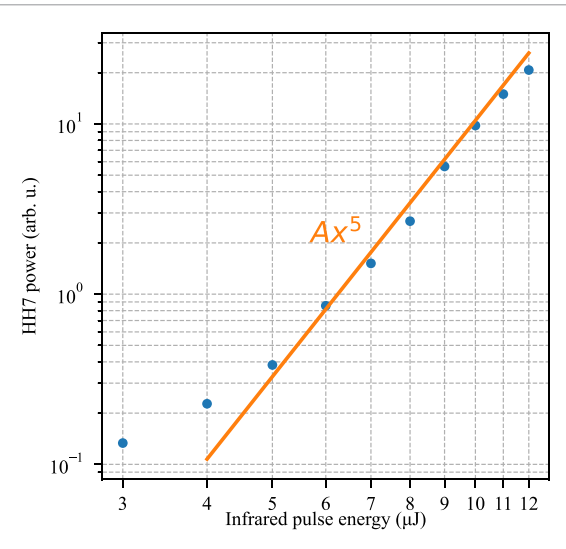


**Figure 4.** Measured power of the 7th harmonic ( $\lambda = 114$  nm) as a function of the infrared pulse energy (blue markers). The orange line is a guide to the eye for a 5th-order polynomial.

the plate, to meta-optics  $(\Delta r < \lambda_0/n)$  in the outskirts of the plate. It provides opportunities to design XUV sources in each of these interaction regimes.

Next, we turn our attention to the XUV field.

#### 3.2. Step 2: high-harmonic emission

The XUV field generated at the top and bottom MgO planes is obtained as a power of the infrared field amplitude ( $|E_{IR}(\vec{r})|$ ), and has m times the phase of the infrared field,  $\phi_0$ :

$$E_{\text{XUV}}(\vec{r}) = |E_{\text{IR}}(\vec{r})|^{j} e^{im\phi_0} \tag{3}$$

The exponent j is obtained from an experimental measurement of the scaling of high-harmonic power with infrared laser power. The laser used is the same as in [30], and has the same parameters (focus size, pulse duration, wavelength) as used in the simulations above. The measured power scaling for the 7th harmonic is shown in figure 4. The closest fit is obtained for j=5. This model neglects the microscopic mechanism of high-harmonic emission such as the existence of an intensity-dependent dipole phase associated with recolliding electron–hole pair trajectories [36, 37]. However, this phase varies smoothly with the intensity, and thus likely affects the focal distance and the trench-to-ridge phase modulation (which, as we shall see, mostly affects the focusing efficiency), but is not expected to significantly change the qualitative behavior of the zone plate. A more refined model will be implemented in follow-up work. Using the measured power scaling and the simulated infrared intensity, the local XUV field at the top ( $E_{\text{XUV}}^{\text{ridge}}(z=0)$ ) and bottom ( $E_{\text{XUV}}^{\text{trench}}(z=-h)$ ) planes is calculated from equation (3). The top field is defined only in regions inside MgO at the top of the ridges (at z=0, yellow areas in figure 2(a)), whereas the bottom field is defined in the complementary areas at z=-h, e.g. at the bottom of the trenches.

Next, the bottom field  $E_{\text{XUV}}^{\text{trench}}(z=-h)$  is propagated a distance h towards the top plane to obtain  $E_{\text{XUV}}^{\text{trench}}(z=0)$ . This is performed with the angular spectrum method [38, 39], which consists of adding the free-space phase along the propagation axis 'z',  $\phi_m = mk_{0,z}h$ , to each plane wave component of the field at the source place (therefore to the Fourier components  $\tilde{E}_{\text{XUV}}^{\text{trench}}(k_x,k_y,z=-h)=\mathcal{F}\{E_{\text{XUV}}^{\text{trench}}(x,y,z=-h)\}$ ), followed by inverse Fourier transformation, which returns the real-space field at z=0,  $E_{\text{XUV}}^{\text{trench}}(z=0)$ . Here,  $k_{0,z}=\vec{k_0}\cdot z$  with  $k_0=2\pi/\lambda_0$ . Therefore:

$$E_{\text{XUV}}^{\text{trench}}(z=0) = \mathcal{F}^{-1} \left\{ \tilde{E}_{\text{XUV}}^{\text{trench}}(k_x, k_y) e^{i\phi_m(k_x, k_y)} \right\}$$
 (4)

$$\phi_m = h\sqrt{\left(\frac{2\pi}{\lambda_m}\right)^2 - k_x^2 - k_y^2}.$$
 (5)

Apart from small differences in the amplitude profile of the propagated field, because of the short propagation distance relative to the high-harmonic wavelength (h = 60 nm,  $\lambda_{m=7} = 114 \text{ nm}$ ) the result is largely equivalent to merely adding the propagation phase  $\phi_m$  with  $k_x = k_y = 0$  to the bottom field. The assumption that the XUV field propagates as in free space, while in reality it is confined within the trenches,

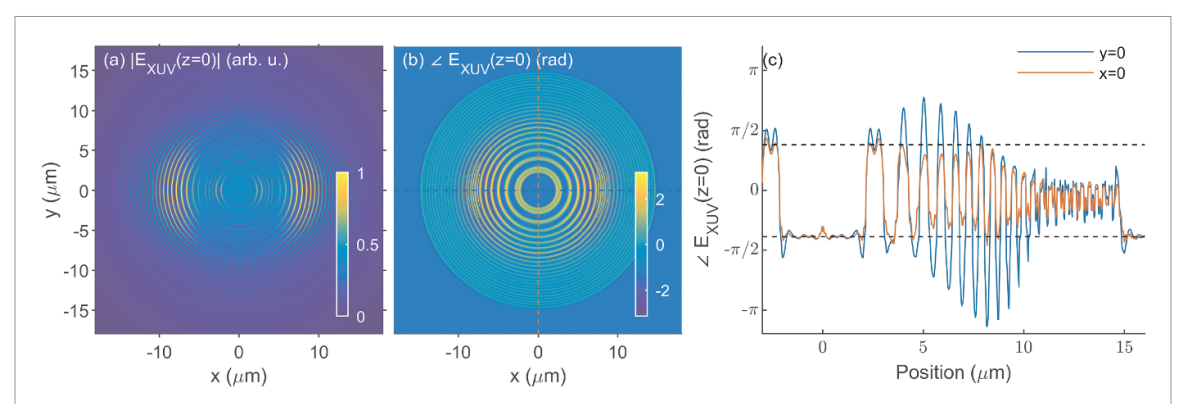


**Figure 5.** Amplitude (panel (a)) and phase (panel (b)) of  $E_{XUV}(z=0)$ . The inhomogeneous distribution is a direct consequence of infrared enhancement. A sizable phase modulation remains for the XUV field even in the sub-wavelength region. (c) Lineouts of the phase. The dashed black lines represent the expected phase modulation from bulk-like features, as obtained with equation (1).

is an approximation that may break down when the trench width becomes comparable to the XUV wavelength. For NA = 0.35, the outermost ring has a width of 164 nm. Thus, resonant scattering or waveguiding effects may not play a role. These effects will be quantified in followup work.

Finally, the field propagated from the bottom of the trenches,  $E_{XUV}^{trench}(z=0)$ , is merged with the field at the top surface originating from the ridges,  $E_{XUV}^{ridge}(z=0)$ :

$$E_{\text{XUV}}(z=0) = \begin{cases} E_{\text{XUV}}^{\text{trench}}(z=0) & \text{in the trenches} \\ E_{\text{XUV}}^{\text{ridge}}(z=0) & \text{in the ridges} \end{cases}$$
 (6)

This procedure removes bottom fields that, due to diffraction, have propagated in regions occupied by the ridges. These fields would be effectively absorbed upon meeting the trench sidewalls, as MgO is strongly absorbing at the harmonics wavelength.

The amplitude and phase of  $E_{XUV}(z=0)$  are shown in figures 5(a) and (b), respectively. Because of the power law in equation (3), modulations in the magnitude of the infrared driver are amplified, which results in a stronger  $\hat{x}$ – $\hat{y}$  asymmetry, and a more pronounced contribution from the enhancement region than from the outer rings. Both asymmetry and enhancement have a sizable effect on the focusing, as will be discussed in the next section. A strategy to homogenize the amplitude across the plate would be to utilize polarization states with cylindrical symmetry, such as an azimuthally or radially polarized infrared driver. As evidenced from figures 2(b) and 5(a), a radially polarized beam seems most appropriate to reduce intensity variations across the plate, and may even result in a smaller focus due to the longitudinal polarization component [40]. Like the amplitude modulation, the phase modulation, figure 5(b), is also amplified by a factor m relative to that of the infrared field. Figures 5(b) and (c) show that the phase asymmetry of the x and y lineouts and modulation depth are strong in the enhancement region. In the sub-wavelength region, on the other hand, phase modulation is much more homogeneous and, albeit reduced, remains a sizable  $\sim$  0.7 rad. In summary, despite the nonlinear response of the structure, the linear-optics design of the zone plate may be effective at focusing XUV radiation. This is confirmed in the next section.

# 3.3. Step 3: propagation of the XUV field to the focus

The field at the top surface,  $E_{XUV}(z=0)$ , is propagated to the focus, z=f, with the angular spectrum method. This method is well suited for this purpose because, contrary to the Fraunhofer and Fresnel integrals, it avoids making use of the paraxial approximation, which would not be applicable here given the large NA. The predicted focus is shown in figure 6(a), and lineouts across y=0 and x=0 are given in panels (b) and (c), blue lines, respectively. The focus of an ideal phase-only Fresnel zone plate is also reported for comparison (dashed black lines). This ideal focus is obtained by propagation of the following XUV field at z=0:

$$E_{\text{XUV}}^{\text{ideal}}(z=0) = \begin{cases} +1 & \text{for } l = 2\eta + 1, \ \eta \in \mathbb{Z}^+ \\ -1 & \text{for } l = 2\eta \end{cases}$$
 (7)

i.e. it consists of a  $[0, \pi]$  phase modulation on every other ring. The  $1/e^2$  radius of the zone plate's focused power is  $(w_{0,x}, w_{0,y}) = (368, 417)$  nm,  $\sim (35\%, 50\%)$  larger than the ideal focus. The larger focus and elliptical shape are likely a result of the combination of field enhancement in the waveguiding region, which effectively lowers the NA of the plate, and of the larger-than- $\pi$  phase modulation in the same region. In

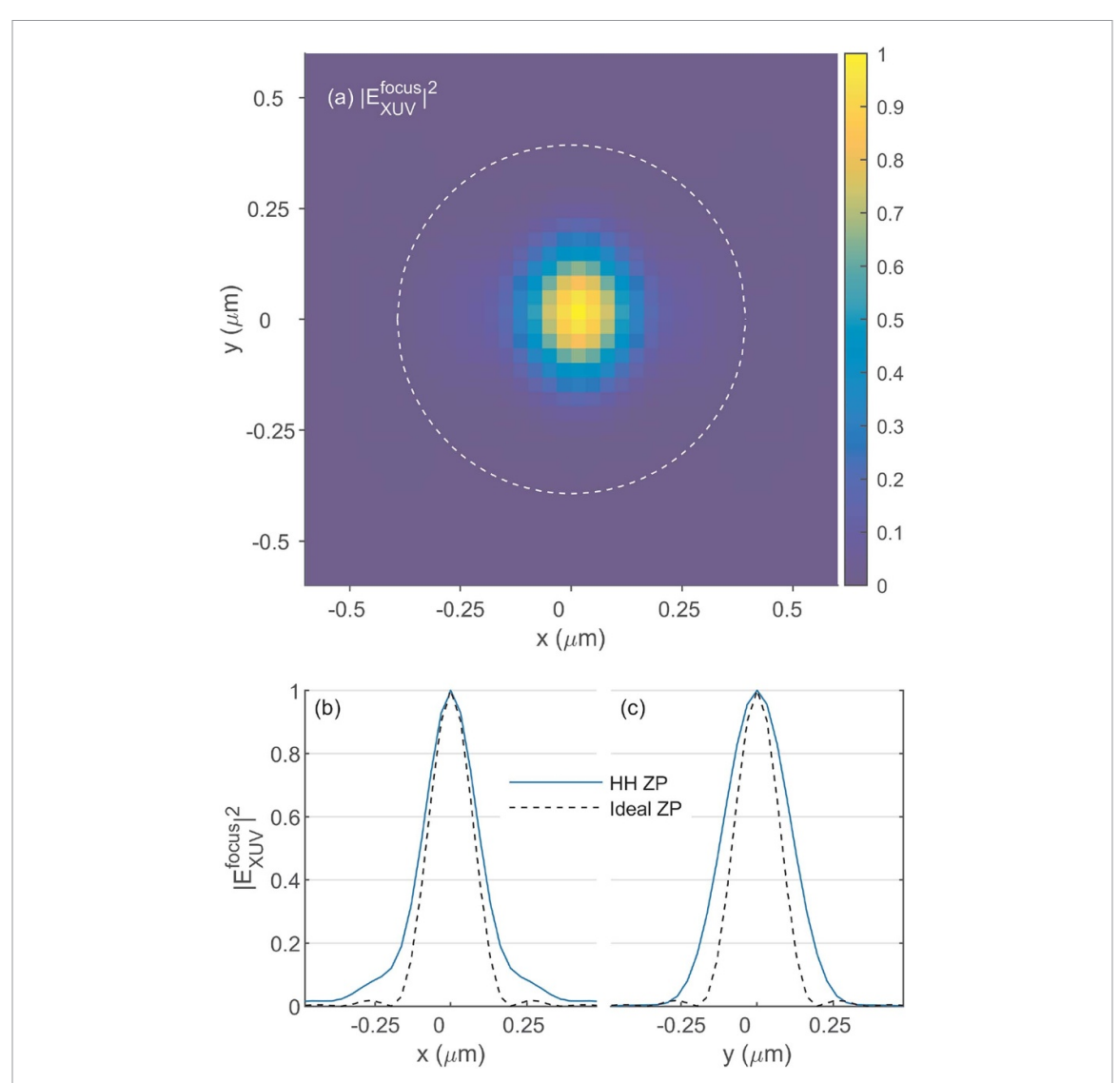


Figure 6. (a) XUV power at the focus. Integrating it inside the white-dashed circle yields the total focused power. (b)–(c) Lineouts across the origin. The black dashed lines show the focus of the ideal phase-only zone plate, with near field defined in equation (7).

addition, figure 7 shows the XUV power of various 2-dimensional slices along the propagation axes. Some minor astigmatism is present. It is, however, remarkable that the pattern of a (linear) Fresnel zone plate operates in a highly nonlinear regime quite effectively. In fact, even the amount of power in the nanofocus relative to the XUV power at the zone plate (the 'focusing efficiency') is quite high, 25%, exceeding that from the ideal plate (18%). The remaining power is primarily in the unfocused zero order, and the rest is either lost to the negative first order or focused to higher orders. The focusing efficiency is obtained by dividing the power integrated over the white dashed circle in figure 6(a) by that integrated over the zone plate diameter in figure 5(a).

In the next section we investigate the focusing of the zone plate with the same topology as in figure 2(a), but as a function of the etch depth, h.

# 4. Etch-depth dependence for NA = 0.35

Table 1 summarizes the simulated focus sizes and focusing efficiencies predicted by our simulations for the various etch depths. Increasing etch depth results in increased field enhancement in the scattering region and in increased phase modulation across the plate. The maximum efficiency of  $\eta=25\%$  is obtained for h=60 nm, notably a higher efficiency than that obtained for the ideal phase-only zone plate, pointing to the fact that the combination of phase and amplitude modulation is somewhat beneficial. For a linear zone plate, the etch depth that should yield the most efficient focusing is the one that results in  $\Delta\phi=\pi$ . Utilizing equation (1), this condition corresponds to h=78 nm, slightly larger than the optimal h. The difference arises from the strong reshaping of the infrared field and from the nonlinearity of the harmonic emission process.

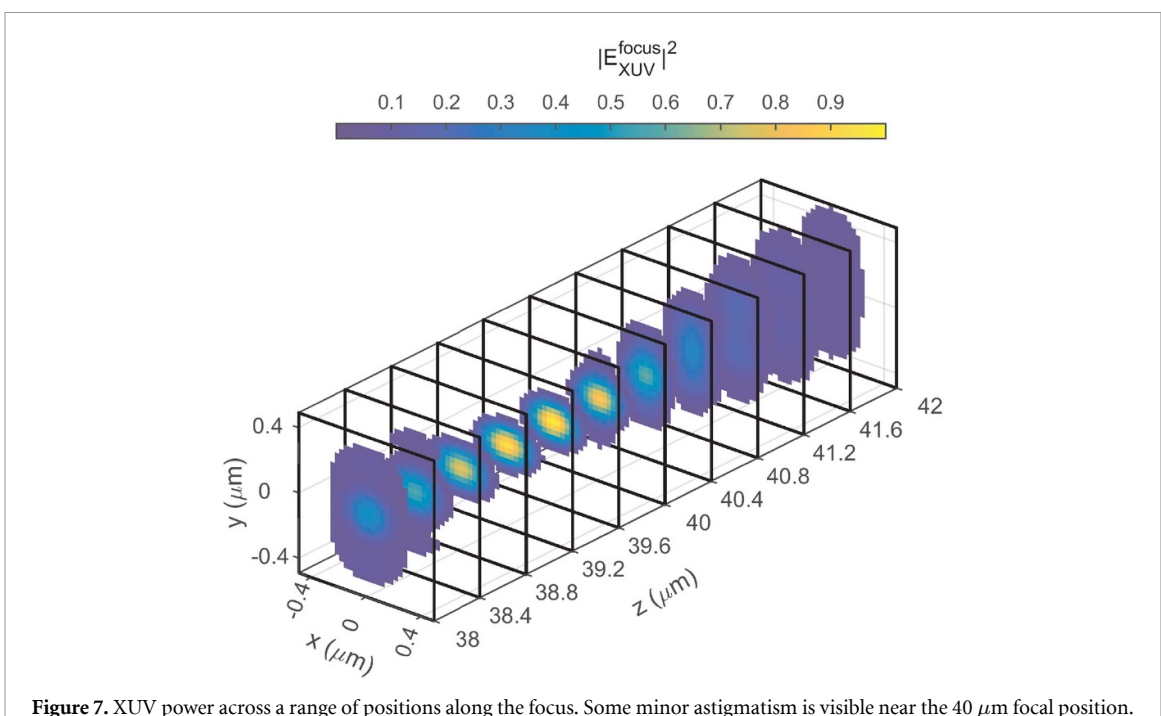


Figure 7. XUV power across a range of positions along the focus. Some minor astigmatism is visible near the 40  $\mu$ m focal position.

**Table 1.** Simulated waist radii across y = 0 ( $w_x$ ) and x = 0 ( $w_y$ ), as obtained from a Gaussian fit, and focusing efficiency  $\eta$  as a function of etch depth h, for the zone plate with NA = 0.35.

$h$ {nm}	$w_x\{nm\}$	$w_y\{nm\}$	$\eta$ {%}
20	445	476	9
40	411	456	18
60	368	417	25
80	341	390	23
100	316	363	16
120	282	343	8
ideal ZP	272	272	18

In the next section we clarify the roles of amplitude and phase modulations.

# 5. Role of amplitude and phase modulations

To understand whether the working principle of the plate described in section 2, based on phase modulation, is responsible for focusing XUV, we simulate the focus obtained with three different artificially modified XUV near-fields,  $E_{\text{mod}}(z=0)$ , for the case h=60 nm.

- (i) First, we neglect any phase modulation, setting  $E_{\text{mod}}(z=0) = |E_{\text{XUV}}(z=0)|$ . The simulated focus, shown in figure 8(a), is severely distorted. Thus, phase modulation is crucial for focusing.
- (ii) Second, we keep the phase modulation of  $E_{XUV}(z=0)$  but set the amplitude to 1:  $E_{mod} = E_{XUV}/|E_{XUV}|$ . The result is shown in figure 8(b). A high-quality focus with  $(w_x, w_y) = (325, 335)$  nm is obtained with a focusing efficiency of  $\eta = 14\%$ , slightly below the 18% limit of the ideal zone plate, which also has a uniform amplitude. The lower efficiency is to be expected, since the phase modulation in the nonlinear plate is not uniformly  $\pi$ . The size of the focus is larger than the ideal zone plate, and slightly elliptical. For the ideal zone plate with a uniform phase modulation, a variation of the modulation depth, h, changes the diffraction efficiency but maintains the focus size. Thus, the larger and elliptical focus size of the modified plate arises from the non-uniformity of the phase modulation. Nonetheless, the ellipticity is less than in figure 6, and the focus is smaller. Therefore, we can conclude that the nonuniform amplitude modulation contributes to worsening the quality of the focus.
- (iii) Finally, we study the effect of the amplitude. We set  $E_{\text{mod}} = |E_{\text{XUV}}| \cdot E_{\text{XUV}}^{\text{ideal}}$ , i.e. the original amplitude is modulated by  $\pm 1$  according to equation (7), corresponding to a  $[0,\pi]$  phase modulation. The result is shown in figure 8(c). The focus size is  $(w_x, w_y) = (299, 342)$ , thus not significantly different from the

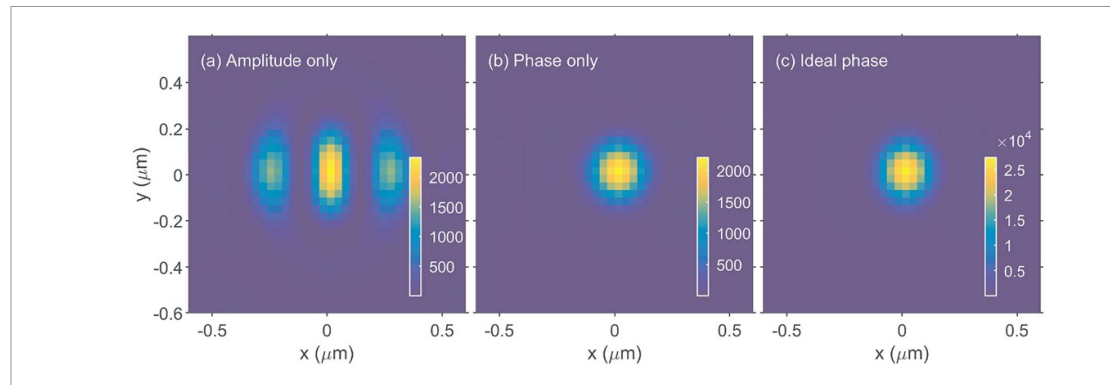


**Figure 8.** Simulated focii for three differently modified XUV fields. (a) Only amplitude modulation of  $E_{\text{XUV}}(z=0)$ . (b)  $E_{\text{XUV}}(z=0)$  with uniform amplitude (only phase modulation). (c) The  $E_{\text{XUV}}(z=0)$  with the phase modulation of the ideal zone plate.

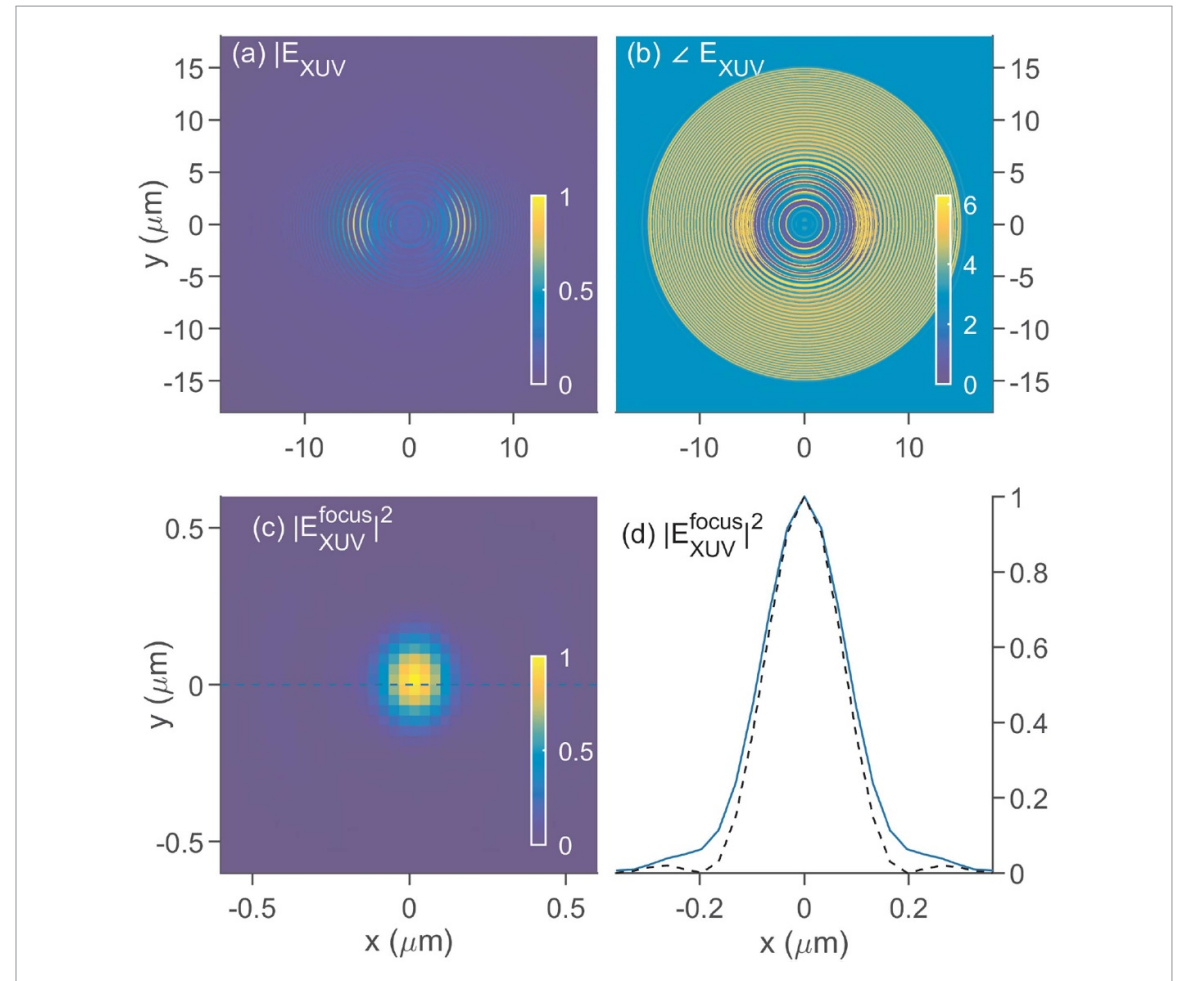


**Figure 9.** Results for a NA = 0.5 zone plate and h = 100 nm. Both field amplitude (panel (a)) and phase (panel (b)) are more uniform. The phase modulation is large throughout the plate. (c) The simulated focus is less elliptical and smaller than for the NA = 0.35 plate. (d) y = 0 lineout of the focused power. The black-dashed line is the focus of the ideal phase-only zone plate.

previous case, but the focusing efficiency is significantly larger,  $\eta = 37\%$ . Thus, amplitude modulations can be quite beneficial.

# 6. NA = 0.5

The quality of the focus improves at higher NAs. Figure 9 shows the results for a zone plate with NA = 0.5 ( $f = 26 \,\mu\text{m}$ ) and  $h = 100 \,\text{nm}$ . Both amplitude and phase profiles (panels (a) and (b), respectively) are much more homogeneous because most of the rings are sub-wavelength relative to the infrared driver, with a

substantial phase modulation of  $\sim$  1.9 rad. The focus (panel (c)) is less elliptical, thanks to the improved homogeneity in the near field, with radius ( $w_x$ ,  $w_y$ ) = (227,258) nm. The ideal phase-only zone plate has  $w_x = w_y = 187$  nm. Lineouts of the focal power across y = 0 are shown in panel (d). The focusing efficiency is  $\eta = 17\%$ , comparable to that for NA = 0.35 (18%). Thus, our approach to nanofocusing high harmonics proves highly effective at the largest NAs achieved with XUV radiation to date [5].

# 7. Conclusions

To conclude, we have developed a numerical model to predict the nonlinear behavior of a nanostructured surface that simultaneously generates and focuses high-order harmonics. The simulations reveal that a linear design based on Fresnel zone plates achieves nanoscale foci with diffraction efficiency that can surpass that of a phase-only Fresnel zone plate. Since phase plates are more efficient than amplitude zone plates, our nonlinear elements outperform transmission XUV zone plates, that typically rely on alternating absorbingtransparent (vacuum) rings. Achieving an adequate phase modulation in the near field is found to be necessary for focusing, and thus a critical aspect for future designs. The addition of a non-uniform amplitude modulation was found to significantly increase the focusing efficiency beyond that of the ideal phase-only Fresnel zone plate. Taken together, our results indicate that there are opportunities to optimize the performance of the device by carefully designing the nanoscale structures to tune both amplitude and phase modulations across the near field, as it is almost certain that the maximum efficiency achieved in this work is not the absolute best. Exploration of such control with sub-wavelength structures (metasurface) is particularly intriguing, and a focus of follow-up work. It can be designed with either forward or inverse (computer-assisted) methods [41]. For example, a smooth quadratic variation of the XUV phase across the device would result in a Fresnel lens, which would focus an XUV beam with a smooth amplitude modulation to the diffraction limit with 100% efficiency.

# Data availability statement

The data cannot be shared publicly at this time due to ongoing analysis as part of a broader study. However, the data that support the findings of this study are available from the authors upon reasonable request.

# Acknowledgment

Financial support provided by the National Research Council Canada and University of Ottawa Joint Center for Extreme Photonics. G V and L R acknowledge support from the National Sciences and Engineering Research Council of Canada.

## **Conflict of interest**

The authors declare no conflicts of interest.

# Author contributions

Parnia Bastani D 0000-0003-2345-4200

Formal analysis (equal), Investigation (equal), Methodology (equal), Writing – original draft (supporting), Writing – review & editing (equal)

Aleksey Korobenko

Methodology (supporting), Writing – review & editing (supporting)

Vedran Jelic D 0000-0003-0020-5156

Formal analysis (supporting), Methodology (supporting), Writing – review & editing (equal)

Jesse Thompson

Formal analysis (supporting), Writing – review & editing (supporting)

Anton Rudenko 🕩 0000-0002-8915-8319

Formal analysis (supporting), Writing – review & editing (supporting)

Francois Légaré

Funding acquisition (supporting), Supervision (supporting)

Lora Ramunno

Funding acquisition (equal), Supervision (equal), Writing – review & editing (equal)

Giulio Vampa

Conceptualization (lead), Formal analysis (equal), Funding acquisition (lead), Methodology (supporting), Supervision (lead), Writing – original draft (lead), Writing – review & editing (lead)

#### References

- [1] Geneaux R, Marroux H J B, Guggenmos A, Neumark D M and Leone S R 2019 Transient absorption spectroscopy using high harmonic generation: a review of ultrafast x-ray dynamics in molecules and solids *Phil. Trans. R. Soc. A* 377 20170463
- [2] Kfir O et al 2017 Nanoscale magnetic imaging using circularly polarized high-harmonic radiation Sci. Adv. 3 eaao4641
- [3] Sandberg R L et al 2007 Lensless diffractive imaging using tabletop coherent high-harmonic soft-x-ray beams Phys. Rev. Lett. 99 098103
- [4] Meng Y, Zhang C, Marceau C, Naumov A Y, Corkum P and Villeneuve D 2015 Octave-spanning hyperspectral coherent diffractive imaging in the extreme ultraviolet range Opt. Express 23 28960–9
- [5] Fu N et al 2019 EUV lithography: state-of-the-art review J. Microelectron. Manuf. 2 19020202
- [6] Schmidt J, Guggenmos A, Hofstetter M, Chew S H and Kleineberg U 2015 Generation of circularly polarized high harmonic radiation using a transmission multilayer quarter waveplate Opt. Express 23 33564–78
- [7] Attwood D 2000 Soft X-rays and Extreme Ultraviolet Radiation: Principles and Applications (Cambridge University Press)
- [8] Ossiander M, Meretska M L, Hampel H K, Lim S W D, Knefz N, Jauk T, Capasso F and Schultze M 2023 Extreme ultraviolet metalens by vacuum guiding Science 380 59–63
- [9] Liu H, Vampa G, Zhang J L, Shi Y, Buddhiraju S, Fan S, Vuckovic J, Bucksbaum P H and Reis D A 2020 Beating absorption in solid-state high harmonics *Commun. Phys.* 3 192
- [10] Ferray M, L'Huillier A, Li X, Lompre L, Mainfray G and Manus C 1988 Multiple-harmonic conversion of 1064 nm radiation in rare gases J. Phys. B: At. Mol. Opt. Phys. 21 L31
- [11] Villeneuve D 2018 Attosecond science Contemp. Phys. 59 47-61
- [12] Luu T T, Yin Z, Jain A, Gaumnitz T, Pertot Y, Ma J and Wörner H J 2018 Extreme—ultraviolet high–harmonic generation in liquids Nat. Commun. 9 3723
- [13] Ghimire S, DiChiara A D, Sistrunk E, Agostini P, DiMauro L F and Reis D A 2011 Observation of high-order harmonic generation in a bulk crystal *Nat. Phys.* 7 138–41
- [14] Ghimire S and Reis D A 2019 High-harmonic generation from solids Nat. Phys. 15 10-16
- [15] Takahashi E J, Kanai T, Ishikawa K L, Nabekawa Y and Midorikawa K 2008 Coherent water window x ray by phase-matched high-order harmonic generation in neutral media Phys. Rev. Lett. 101 253901
- [16] Li J et al 2017 53-attosecond x-ray pulses reach the carbon k-edge Nat. Commun. 8 186
- [17] Cardin V, Schmidt B, Thiré N, Beaulieu S, Wanie V, Negro M, Vozzi C, Tosa V and Légaré F 2018 Self-channelled high harmonic generation of water window soft x-rays J. Phys. B: At. Mol. Opt. Phys. 51 174004
- [18] Teichmann S M, Silva F, Cousin S, Hemmer M and Biegert J 2016 0.5-kev soft x-ray attosecond continua Nat. Commun. 7 11493
- [19] Luu T T, Garg M, Kruchinin S Y, Moulet A, Hassan M T and Goulielmakis E 2015 Extreme ultraviolet high-harmonic spectroscopy of solids Nature 521 498–502
- [20] Sivis M, Taucer M, Vampa G, Johnston K, Staudte A, Naumov A Y, Villeneuve D, Ropers C and Corkum P 2017 Tailored semiconductors for high-harmonic optoelectronics Science 357 303–6
- [21] Han S, Kim H, Kim Y W, Kim Y-J, Kim S, Park I-Y and Kim S-W 2016 High-harmonic generation by field enhanced femtosecond pulses in metal-sapphire nanostructure *Nat. Commun.* 7 13105
- [22] Vampa G et al 2017 Plasmon-enhanced high-harmonic generation from silicon Nat. Phys. 13 659-62
- [23] Liu H, Guo C, Vampa G, Zhang J L, Sarmiento T, Xiao M, Bucksbaum P H, Vučković J, Fan S and Reis D A 2018 Enhanced high-harmonic generation from an all-dielectric metasurface *Nat. Phys.* 14 1006–10
- [24] Zograf G et al 2022 High-harmonic generation from resonant dielectric metasurfaces empowered by bound states in the continuum ACS Photonics 9 567–74
- [25] Shcherbakov M R et al 2021 Generation of even and odd high harmonics in resonant metasurfaces using single and multiple ultra-intense laser pulses Nat. Commun. 12 4185
- [26] Jalil S A et al 2022 Controlling the polarization and phase of high-order harmonics with a plasmonic metasurface Optica 9 987–91
- [27] You Y S, Reis D A and Ghimire S 2017 Anisotropic high-harmonic generation in bulk crystals Nat. Phys. 13 345-9
- [28] Korobenko A, Hammond T, Zhang C, Naumov A Y, Villeneuve D and Corkum P 2019 High-harmonic generation in solids driven by counter-propagating pulses Opt. Express 27 32630-7
- [29] Korobenko A, Rashid S, Heide C, Naumov A Y, Reis D, Berini P, Corkum P and Vampa G 2021 Generation of structured coherent extreme ultraviolet beams from an MgO crystal Opt. Express 29 24161–8
- [30] Korobenko A, Rashid S, Heide C, Naumov A Y, Reis D A, Berini P, Corkum P B and Vampa G 2022 In-situ nanoscale focusing of extreme ultraviolet solid-state high harmonics Phys. Rev. X 12 041036
- [31] Okamoto K 2021 Fundamentals of Optical Waveguides (Elsevier)
- [32] Kivshar Y 2018 All-dielectric meta-optics and non-linear nanophotonics Natl Sci. Rev. 5 144-58
- [33] Ding F, Pors A and Bozhevolnyi S I 2017 Gradient metasurfaces: a review of fundamentals and applications Rep. Prog. Phys. 81 026401
- [34] Chen W T, Zhu A Y, Sanjeev V, Khorasaninejad M, Shi Z, Lee E and Capasso F 2018 A broadband achromatic metalens for focusing and imaging in the visible *Nat. Nanotechnol.* 13 220–6
- [35] Wang S et al 2018 A broadband achromatic metalens in the visible Nat. Nanotechnol. 13 227-32
- [36] Vampa G, McDonald C, Orlando G, Klug D, Corkum P and Brabec T 2014 Theoretical analysis of high-harmonic generation in solids Phys. Rev. Lett. 113 073901

- [37] Vampa G, McDonald C, Orlando G, Corkum P and Brabec T 2015 Semiclassical analysis of high harmonic generation in bulk crystals *Phys. Rev. B* **91** 064302
- [38] Goodman J W 2005 Introduction to Fourier Optics (Roberts and Company publishers)
- [39] Kim Y-H, Kim G H, Ryu H, Chu H-Y and Hwang C-S 2015 Exact light propagation between rotated planes using non-uniform sampling and angular spectrum method *Opt. Commun.* 344 1–6
- [40] Dorn R, Quabis S and Leuchs G 2003 Sharper focus for a radially polarized light beam *Phys. Rev. Lett.* 91 233901
- [41] Molesky S, Lin Z, Piggott A Y, Jin W, Vucković J and Rodriguez A W 2018 Inverse design in nanophotonics Nat. Photon. 12 659–70